

Doubling the power efficiency of radioluminescent batteries via tuning the optical filed*

Chen Zhao,^{1,2} Hai-Bin Li,^{1,2} Yin-Ke Liu,^{1,2} Yun-Tao Wu,³ and Yi-Ying Zhao^{1,2,†}

¹Institute of Materials, China Academy of Engineering Physics, Jiangyou, 621908, China

²Sichuan Provincial Engineering Research Center of Deuterium-Tritium Fuel Cycle, Chengdu, 610299, China

³Artificial Crystal Research Center, Shanghai Institute of Ceramics,
Chinese Academy of Sciences, Shanghai 201899, China

Radioluminescent (RL) batteries, offering exceptional energy density and extended operational lifetime, hold significant promise for applications in remote and extreme environments such as aerospace and deep-sea exploration. However, their widespread applications have been hindered by low energy conversion efficiency, primarily stemming from the poor optical outcoupling. In this work, we successfully doubled the efficiency of $Cs_3Cu_2I_5$: Tl -based X-ray RL batteries through systematic optical field engineering. A reflective film was applied on the top and side surfaces of the scintillator to minimize light losses. An optocoupler adhesive was adopted to realize refractive index matching between the scintillator and the photovoltaic cell, which not only shortens the light propagation path within the scintillator but also minimizes self-absorption losses. As a result, the optical coupling efficiency was improved from 22.9% to 51.0%, leading to a 133.7% enhancement in overall device performance. The optimized battery achieves a power conversion efficiency of 2.15% and an output power density of $12.9 \mu W/cm^2$. This study not only underscores the critical role of optical field management in advancing RL battery technology but also provides a strategic pathway for unlocking the full potential of RL batteries.

Keywords: Isotope battery, Radioluminescent battery, Scintillator, Outcoupling efficiency, Power conversion efficiency

I. INTRODUCTION

Radioluminescent (RL) photovoltaic batteries have recently garnered increasing research attention due to their unique advantages, including extremely high energy density, and ultralong lifetime [1–5]. These attributes make them particularly attractive for powering micro-electromechanical systems (MEMS) and aerospace electronics in extreme environments where reliability and longevity are of paramount importance[6–8]. However, unlike direct-conversion radio-voltaic batteries[9–11], RL batteries operate via an indirect energy conversion scheme. The ionizing radiation is first converted into visible light within a scintillator, which is then harvested by a photovoltaic unit to generate electricity. This two-step process inherently introduces additional energy loss pathways, placing RL batteries at a comparative disadvantage in terms of overall energy conversion efficiency[12, 13]. Therefore, improving the energy conversion efficiency has emerged as the most critical research priority for advancing the practical application of RL battery.

Previous efforts to enhance the overall conversion efficiency of RL batteries have focused on optimizing the scintillator, primarily through two strategies: improving the intrinsic radio-luminescence efficiency of scintillator materials and enhancing the light collection efficiency[14–20]. As for novel scintillator materials, zero-dimensional copper-based halides, particularly $Cs_3Cu_2I_5$, have emerged as promising candidates for RL battery applications due to their high light yield[21–29]. Zeng et al. introduced Mn^{2+} -doped $Cs_3Cu_2I_5$ scintillators, achieving a light yield of 67,000

photons/MeV and demonstrating an output power density of $0.46 \mu W/cm^2$ in a prototype RL battery[30]. Subsequently, Ouyang et al. reported a high-performance RL nuclear battery based on ultrabright $Cs_3Cu_2I_5$: Tl single crystal scintillators, attaining an output power of $0.9 \mu W/cm^2$, which surpassed the performance of batteries employing conventional ZnS: Ag and LYSO: Ce scintillators[31]. Parallel efforts have been directed toward improving light collection efficiency. Xu et al. conducted systematic investigations on the scintillator-photovoltaic interface, demonstrating that a silver nanosphere array deposited on the photovoltaic cell surface enhances forward scattering of RL photons, thereby increasing the light absorption by up to 43.66% and boosting electrical output by 44.91%[32]. They also proposed incorporating a SiO_2 nanosphere coating within the fluorescent layer to address weak radioluminescence, achieving a 51.59% improvement in maximum output power[33]. Separately, San et al. explored the role of reflective layers on the scintillator surface, systematically investigating the effect of reflective layer type and thickness. Their results showed that a 100 nm thick Ag film yielded a 52.6% enhancement in RL battery efficiency[34]. Overall, all studies focusing on the optimization of scintillators in RL batteries have demonstrated promising results.

Our previous work has theoretically identified that the energy conversion efficiency within the scintillator remains the primary bottleneck in RL battery performance[35]. Moreover, among the various loss mechanisms, the optical outcoupling efficiency of the scintillator emerges as the most critical factor requiring immediate improvement. However, no systematic investigation has been done to specifically address and improve the optical outcoupling efficiency in RL batteries. In particular, the mechanisms by which the reflection layer and the scintillator-photovoltaic interface affect the optical losses within the scintillator remain poorly understood. The details of optical field regulation require further targeted

* Supported by the National Natural Science Foundation of China (No. 12275243, No. 12305403 and No. U2436201)

† Corresponding author, zhaoyiying@caep.cn

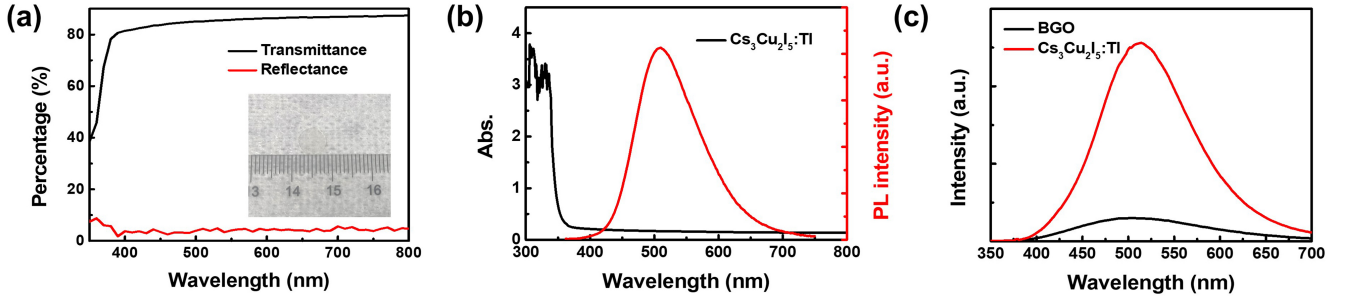


Fig. 1. (a) Transmission and reflection spectrum of a 0.6-mm-thick $Cs_3Cu_2I_5 : Tl$ single crystal scintillator, inset: photograph of the $Cs_3Cu_2I_5 : Tl$ single crystal scintillator; (b) UV-vis absorption (black line) and PL emission (red line) spectra of the $Cs_3Cu_2I_5 : Tl$ single crystal scintillator; (c) RL spectra of $Cs_3Cu_2I_5 : Tl$ and BGO scintillator under the radiation of an X-ray tube biased at 20 kV.

optimization to maximize the overall efficiency enhancement of RL batteries. To address this gap, this study establishes a comprehensive Monte Carlo multi-physics coupling model for the most promising $Cs_3Cu_2I_5 : Tl$ -based X-ray RL battery. This model enables quantitative analysis of the optical outcoupling efficiency and systematically clarifies the loss mitigation mechanisms enabled by the reflection layer and the optical outcoupling layer. Through the synergistic optimization of self-absorption losses and surface optical losses, we successfully achieve a doubling of the battery's overall energy conversion efficiency.

II. MATERIALS AND METHODS

A. Optical and RL properties of $Cs_3Cu_2I_5 : Tl$ SC

The Tl-doped $Cs_3Cu_2I_5$ single crystal was selected as the scintillator material in this study for the X-ray RL battery, owing to its high light yield and low self-absorption, as reported in previous paper. A systematic investigation of the optical and RL properties of the $Cs_3Cu_2I_5 : Tl$ scintillator including light yield, refractive index, and absorption coefficient, was conducted to obtain all the key optical parameters of the scintillators as inputs for the Geant4 simulation model. Fig. 1(a) presents the transmission and reflection spectra of a 0.6 mm-thick, 3.5 mm-radius $Cs_3Cu_2I_5 : Tl$ single-crystal scintillator. The scintillator exhibits high transmittance, reaching approximately 85% across the entire visible spectrum. Based on the average transmittance, the refractive index was determined to be 1.796. A decline in transmittance is observed at wavelengths below 350 nm, which is attributed to the interband absorption. Furthermore, the reflectance remains around 3% within the 300–800 nm range, indicating a smooth and optically uniform surface. Based on the absorption spectrum, the absorption coefficient of the $Cs_3Cu_2I_5 : Tl$ scintillator was calculated to be 0.089 mm^{-1} .

Fig. 1(b) shows the UV-visible absorption (black line) and photoluminescence (PL) emission (red line) spectra of the $Cs_3Cu_2I_5 : Tl$ single-crystal scintillator, with an excita-

tion wavelength of 350 nm. The scintillator exhibits a strong absorption peak at approximately 350 nm and a broad green emission band ranging from 400 nm to 750 nm, centered at around 510 nm with a full width at half maximum (FWHM) of 110 nm. The observed Stokes shift is about 160 nm, indicating a low self-absorption characteristic, which meets perfectly the material requirements of X-ray RL batteries.

Fig. 1(c) presents the radioluminescence (RL) spectra of $Cs_3Cu_2I_5 : Tl$ and a BGO scintillator under X-ray irradiation from a tube operated at 20 kV. The RL spectrum of the $Cs_3Cu_2I_5 : Tl$ scintillator exhibits the same spectral range and peak position as its photoluminescence (PL) spectrum. At this tube voltage, both scintillators fully absorb the incident X-ray energy. The $Cs_3Cu_2I_5 : Tl$ scintillator demonstrates significantly higher RL intensity compared to the BGO scintillator, which has a standard light yield of 8000 photons/MeV. Accordingly, the light yield of the $Cs_3Cu_2I_5 : Tl$ scintillator is calculated to be 50,000 photons/MeV. Through the systematic characterization of the optical and RL properties of $Cs_3Cu_2I_5 : Tl$, as summarized in Fig. 2, key parameters including light yield, refractive index, and absorption coefficient have been determined and can be directly utilized as inputs for the Geant4 simulation model.

B. Establishment of the Geant4 Monte Carlo model

The physical processes of light emission and outcoupling in the scintillator of the RL battery are schematically illustrated in Fig. 2(a). The X-rays incident into the scintillator and excite the free electrons, with the cost of the ionized energy of the scintillator. The free electrons relax to the ground states of the conduction band of the scintillator and then hop to the excited energy levels of the doped activators, which will radiatively recombine and emit light. The optical photons will either be self-absorbed or escape from all surfaces of the scintillator, among which only the part emitted from the bottom surface can be outcoupled into the photovoltaic unit and converted into electrons. The light emission and propagation processes are illustrated in the left and right part of Fig. 2(a), respectively. The quantum efficiency and energy

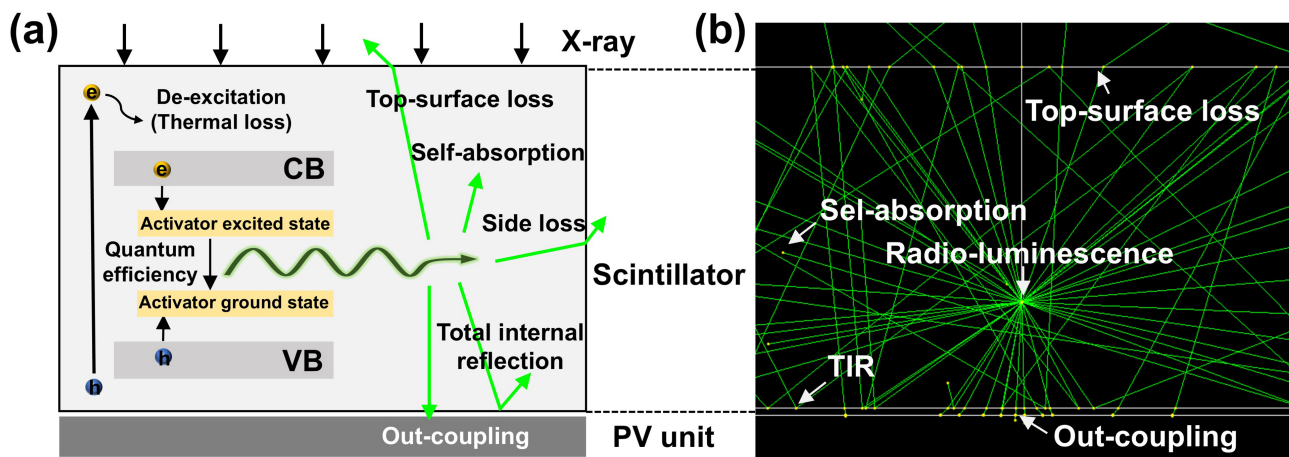


Fig. 2. (a) Diagram of the energy conversion process in an X-ray RL battery, illustrating the radio-luminescence and optical loss mechanisms; (b) Energy dissipation process of optical photons in RL battery simulated using the Geant4 Monte Carlo model, where white lines stand for the trajectory of X-rays, green lines for optical photons, and yellow spots for the energy loss events.

loss of the RL process strongly depends on the properties of the scintillators, which is not in the scope of this work. This work mainly focuses on the dominating factors which is not related to the properties of scintillators in the RL battery.

The ratio of photon energy dissipated into each mode can be calculated using the Geant4 simulation. The RL battery model incorporating both the radiation and optical fields is presented in Fig. 2(b). The X-ray spectrum emitted from the X-ray tube was calculated by Spekpy and used to mimic the spectrum of the X-ray source in the Monte Carlo simulation. 10000 X-ray photons were used in each simulation. The electromagnetic interactions between X-rays and scintillators were simulated using a custom model that accounts into all the key physical processes, including the photoelectric effect, Compton scattering, Rayleigh scattering, and electron pair production. The built-in model in Geant4 software registering the optical properties of the scintillator and the photovoltaic unit (including light yield, refractive index, and absorption coefficient etc.) is employed to simulate all the optical process. The unified model is chosen to as the optical boundary conditions and used to simulate all optical surfaces. As illustrated in Fig. 2(b), white lines stand for the trajectory of X-rays and green lines trace the paths of optical photons generated within the scintillator. Photons either undergo the total internal reflection (TIR) or transmit into the PV unit (representing coupled light) or escape to the atmosphere (representing light leakage), when encounter the surfaces, i.e. the optical boundaries. The scattering processes are not considered in the simulation, since the scintillator used in this study is transparent single-crystal (SC). Part of the photons can also be absorbed at the defects, which is presented as yellow spots for the energy loss events. As shown in the simulation, the optical photons will either be self-absorbed or escape from all surfaces of the scintillator, among which only the part emitted from the bottom surface can be outcoupled into the photovoltaic unit and converted into electrons.

C. Validation of the model

To verify the accuracy of the established multi-physics coupling model, CsI:Tl single crystal scintillators were employed for experimental validation. Fig. 3(a) presents five CsI:Tl samples with thicknesses ranging from 0.2 mm to 1.0 mm. These scintillators with varying thicknesses will exhibit differences in X-ray absorption and RL self-absorption, making them suitable for benchmarking the model predictions. The transmission spectra of the five CsI:Tl scintillators are shown in Fig. 3(a), revealing reduced optical transparency with increasing thickness. Based on these transmission curves, the self-absorption coefficient of the CsI:Tl scintillator material was extracted by fitting the linear relationship between $\lg(1/T)$ and thickness d . The fitting results, displayed in Fig. 3(b), yield a self-absorption coefficient of 0.0418 mm^{-1} .

To investigate the RL response of CsI:Tl scintillators with varying thicknesses, measurements were performed under X-ray irradiation at different tube voltages, with the results presented in Fig. 3(c). At low tube voltages, the RL intensity of the CsI:Tl scintillator increases with thickness. As the tube voltage rises, however, the RL intensity exhibits a trend of first increasing and then decreasing with thickness. Specifically, at a tube voltage of 30 kV, the scintillator with a thickness of 0.4 mm yields the highest RL intensity, whereas at 40 kV and 50 kV, the maximum fluorescence intensity is observed for the 0.6 mm thick sample. This trend reflects the trade-off between X-ray absorption and light self-absorption: increasing the scintillator thickness enhances X-ray absorption but also leads to greater optical losses due to self-absorption. At lower tube voltages, the effect of thickness on X-ray absorption is less pronounced. At higher voltages, the increased penetration depth results in reduced RL intensity for thinner scintillators. Fig. 3(d) displays the corresponding simulation results obtained from the theoretical

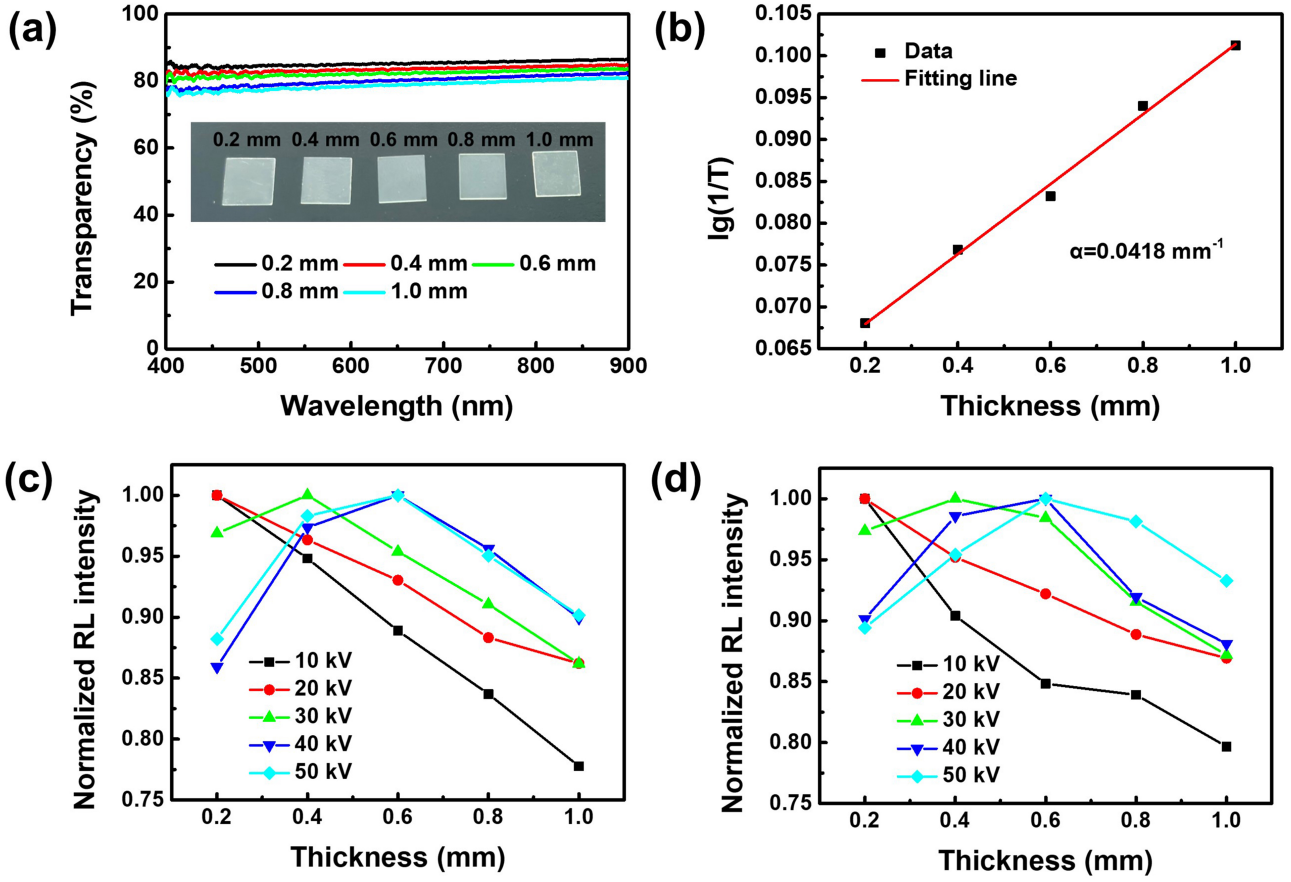


Fig. 3. (a) Transmission spectra of CsI:Tl single crystal scintillators with different thicknesses; (b) Fitting of absorption coefficients for CsI:Tl single crystal scintillators; (c) Measured and (d) simulated changes in radioluminescence intensity of CsI:Tl scintillators with different thicknesses under different X-ray tube voltages.

model. The modeled trends are in excellent agreement with the experimental observations, and the normalized RL intensity variations closely match the measured data. These findings confirm the reliability and predictive capability of the developed model.

III. RESULTS AND DISCUSSIONS

A. Optical loss modes in X-ray Battery

Fig. 4(a) presents a schematic diagram of the measurement setup for the X-ray RL battery. An X-ray tube with a tungsten target (Oxford, Apogee 5500) was employed to mimic a low-energy X-ray radioactive source, owing to its advantageous features such as a steerable irradiation area, adjustable X-ray flux, and minimal radiation protection requirements. The $Cs_3Cu_2I_5$: Tl scintillator and a GaInP photovoltaic unit, with a bandgap of 1.84 eV, were positioned directly beneath the X-ray tube. The size of the GaInP PV unit is one centimeter square, which is larger than the $Cs_3Cu_2I_5$: Tl scintillator. In order to avoid the impact of direct X-ray irra-

diation on the GaInP PV unit, a collimator was used to ensure that the X-ray irradiation area is on the $Cs_3Cu_2I_5$: Tl scintillator. In order to maximize the output power of the X-ray RL battery, the tube was operated at the highest tube voltage of 50 kV. The spectrum of X-ray with 50 kV tube voltage was measured using a SDD detector as shown in Fig. 4(a). The spectrum shows the L-series characteristic peaks of tungsten at 8.4 keV, 9.7 keV and 11.3 keV, and the average energy of X-rays is 14.5 keV. The measured X-ray spectrum was used to calculate the energy deposition profile and the absorbed energy ratio within the $Cs_3Cu_2I_5$: Tl scintillator, as illustrated in Fig. 4(b). The energy deposition exhibits an exponential decay profile, and it was determined that a 0.6 mm-thick $Cs_3Cu_2I_5$: Tl scintillator absorbs 96.4% of the incident X-ray energy.

The inset in Fig. 4(c) illustrates the spectral matching between the external quantum efficiency (EQE) of the GaInP photovoltaic unit and the radioluminescence (RL) spectrum of the $Cs_3Cu_2I_5$: Tl scintillator. The cutoff edge of the GaInP EQE spectrum is slightly lower than that of the RL emission from the scintillator. In accordance with the method for optimizing the bandgap of photovoltaic units reported in our previous work, the 1.84 eV GaInP cell represents

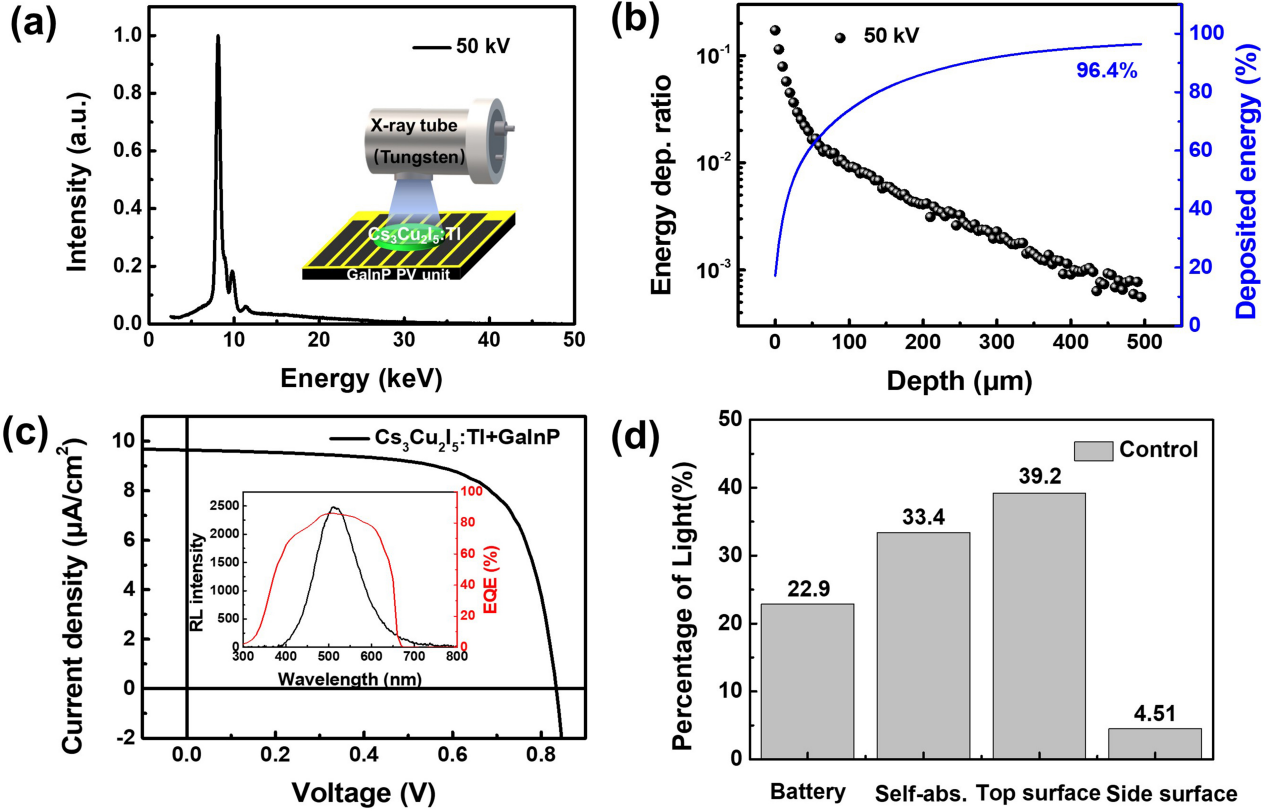


Fig. 4. (a) Measured X-ray spectrum of an X-ray tube operated at 50 kV, Inset: schematic diagram of measurement scheme of X-ray RL battery based on $Cs_3Cu_2I_5 : Tl$ single crystal scintillator using an X-ray tube; (b) Energy deposition profile and deposited energy ratio in $Cs_3Cu_2I_5 : Tl$ scintillators under the radiation of an X-ray tube biased at 50 kV, where 96.4% of the total energy is deposited in 0.6 mm; (c) Current density-voltage (J-V) curves of X-ray RL battery based on $Cs_3Cu_2I_5 : Tl$ scintillator and GaInP photovoltaic unit under the radiation of an X-ray tube biased at 50 kV and with a tube current of 1mA; Inset: Spectral matching between the RL spectrum of $Cs_3Cu_2I_5 : Tl$ scintillator and EQEs of GaInP photovoltaic unit with a bandgap of 1.84 eV; (d) Quantitative analysis of different optical loss mechanisms in the battery.

a balance between photon absorption and output voltage, thereby maximizing the power output of the X-ray RL battery. Fig. 4(c) displays the current density-voltage (J-V) characteristics of the X-ray RL battery, comprising the $Cs_3Cu_2I_5 : Tl$ scintillator and the GaInP photovoltaic unit, under X-ray irradiation at 50 kV and 1.0 mA. The device exhibits a short-circuit current density (J_{sc}) of $9.6 \mu A/cm^2$, an open-circuit voltage (V_{oc}) of 0.834 V, a fill factor (FF) of 68.5%, a maximum output power density (P_{out}) of $5.51 \mu W/cm^2$, and an energy conversion efficiency (η) of 0.92%.

and the absorption coefficient of the scintillator. Once the scintillator material is selected, this loss can only be reduced by minimizing the total optical path length. An outcoupling efficiency of 22.9% implies that roughly one in four photons reach the photovoltaic unit. This efficiency can be improved by mitigating top and side surface losses and enhancing light extraction at the bottom interface.

B. Reflection film to reduce the light leakage in scintillators

In order to mitigate optical losses from the top and side surfaces of the $Cs_3Cu_2I_5 : Tl$ scintillator, three types of reflective films were evaluated: a $20 \mu m$ thick aluminum foil (#1), a $20 \mu m$ Al-coated PET film with a $1 \mu m$ aluminum layer (#2), and a $65 \mu m$ thick organic reflective film (#3, ESR, 3M). The inset in the figure shows the photograph of these three kinds of reflection films. Aluminum foil was selected as a commonly used reflector in RL batteries due to its high reflectivity. However, to reduce the energy absorption of

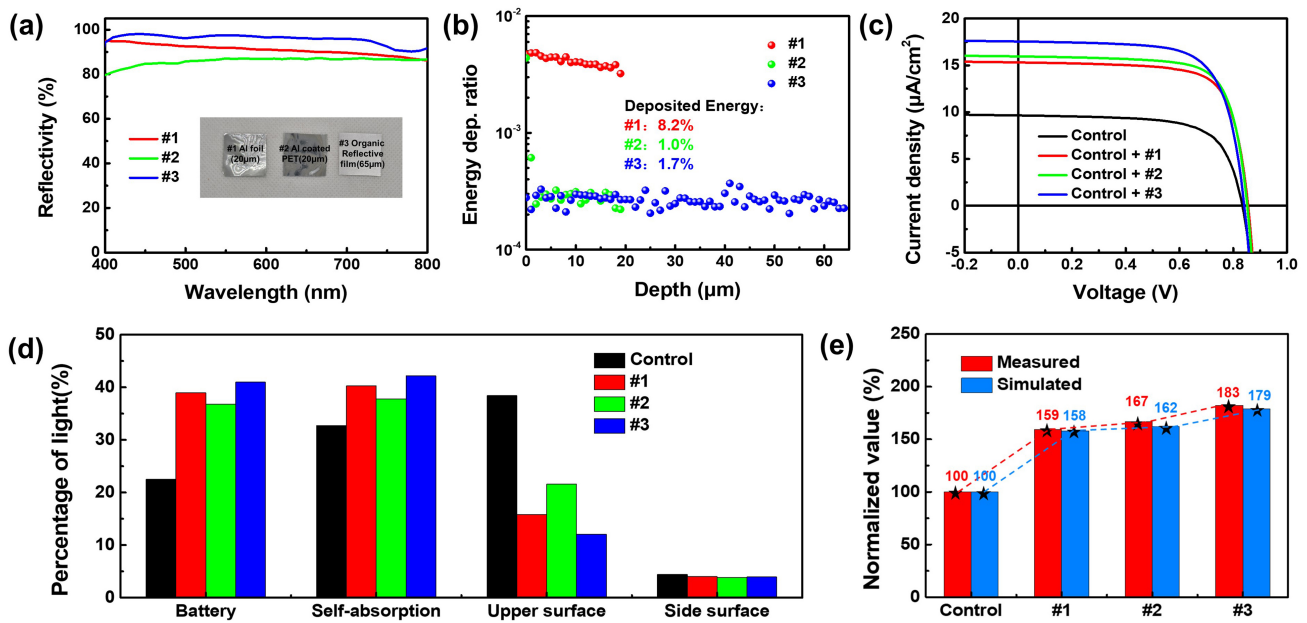


Fig. 5. (a) Reflection spectra of three different kinds of reflection films including a 20 μm aluminum foil (#1), a 20 μm Al-coated PET film (#2), and a 65 μm Organic Reflection film (#3); (b) Energy deposition profiles in three kinds of reflection layers under the radiation of an X-ray tube biased at 50 kV; (c) Current density-voltage (J-V) characteristic curves of the RL battery with no addition reflection layer and three kinds of reflection layers measured under the radiation of an X-ray tube biased at 50 kV and with a tube current of 1 mA; (d) Quantitative analysis of different optical loss mechanisms in the four battery configurations; (e) Comparison of the measured short-circuit currents and the calculated incident light intensities of the batteries with four configurations.

X-rays, which is influenced by the effective atomic number, an Al-coated PET film was also investigated, as PET offers a lower effective atomic number compared to aluminum. Furthermore, a fully organic reflective film was included to minimize both X-ray energy loss and surface plasmon resonance (SPR)-induced optical loss. Fig. 5(a) displays the reflection spectra of the three reflective films. The organic reflective film exhibits the highest average reflectivity of 95.7%. The aluminum foil shows a slightly lower average reflectivity of 91.0%, which can be attributed to SPR loss. In contrast, the Al-coated PET film demonstrates the lowest average reflectivity of 85.9%, resulting from the thinness of the aluminum coating.

In addition to reflectivity, the energy loss of X-rays within the reflective films also significantly influences the overall output performance of the X-ray RL battery. Fig. 5(b) presents the energy deposition profiles in the three types of reflective layers under irradiation from an X-ray tube operated at 50 kV. The aluminum foil exhibits the highest energy deposition, with 8.2% of the incident X-ray energy being absorbed within it. The Al-coated PET film shows a similar deposition profile to the aluminum foil within the first 1 μm , corresponding to the aluminum layer, followed by a rapid decrease across the PET substrate. The total energy deposition in the Al-coated PET film is 1.0%, which is substantially lower than that of the pure aluminum foil. The organic reflective film maintains a low energy deposition throughout its entire thickness; however, due to its greater thickness of

65 μm , the total energy deposition (1.7%) is slightly higher than that of Al-coated PET film. The output performance of the RL battery was evaluated both without any reflective layer and with each of the three types of reflective layers under X-ray irradiation at 50 kV and 1 mA tube current. The current density-voltage (J-V) characteristics for these four configurations are presented in Fig. 5(c). It is evident that the use of any reflective film leads to a significant improvement in performance compared to the control configuration without a reflector. Among the four configurations, the RL battery equipped with reflective film #3 demonstrates the highest performance. The corresponding output parameters are summarized in Table 1. The enhancement in battery performance is primarily attributed to an increase in short-circuit current density (J_{sc}). The J_{sc} values for batteries with reflective films #1, #2, and #3 are 15.3, 16.0, and 17.5 $\mu\text{A}/\text{cm}^2$, respectively, resulting in energy conversion efficiencies of 1.60%, 1.68%, and 1.75%. The organic reflective film (#3), which combines low X-ray absorption with the highest reflectivity, contributes to a 90% improvement in the energy conversion efficiency of the X-ray RL battery compared to the non-reflective configuration.

A quantitative analysis of the optical loss mechanisms in the four battery configurations (without any reflective layer and with each of the three reflective films) was performed using Geant4 simulations. As illustrated in Fig. 5(d), the percentage of light coupled into the PV unit is 22.4% for the control configuration, and 38.9%, 36.8%, and 41.0% for the

TABLE 1. Output parameters of RL batteries with different reflection films

Sample	$J_{sc}(\mu A/cm^2)$	$V_{oc}(V)$	FF(%)	$P_{out}(\mu W/cm^2)$	$\eta(\%)$
Control	9.6	0.834	68.5	5.51	0.92
#1	15.3	0.855	73.2	9.58	1.60
#2	16.0	0.852	73.7	10.0	1.68
#3	17.5	0.841	70.8	10.4	1.75

batteries with reflective films #1, #2, and #3, respectively. The introduction of a reflective film effectively reduces optical loss at the top and side surfaces, thereby substantially enhancing the outcoupling efficiency. The degree of improvement correlates with the reflectivity of the film. The organic reflective film (#3), which possesses the highest reflectivity, reduces top-surface loss from 38.4% to 12.0%. In contrast, the Al-coated PET film (#2), with the lowest reflectivity, only reduces top-surface loss to 21.6%. However, the presence of the reflective film also prolongs the average light path within the scintillator, leading to a moderate increase in self-absorption loss. For instance, when the organic reflective film is used, self-absorption rises from 32.7% to 42.2%. In summary, the primary benefit of incorporating a reflective film lies in its ability to mitigate light escape from the top and sides, which markedly improves optical coupling efficiency. The organic reflective film, in particular, achieves an 83% improvement in outcoupling efficiency compared to the control configuration.

To assess the accuracy of the simulation results, the measured short-circuit current densities and the calculated incident light intensities were compared across the four battery configurations. Given that the external quantum efficiency (EQE) of the PV units remains nearly constant across the light intensity ranges studied in this work, the short-circuit current density can be considered proportional to the incident light intensity. Accordingly, both the measured current densities and the simulated incident light intensities for all configurations were normalized to those of the control device and are presented in Fig. 5(e). The measured current densities for batteries equipped with reflective films #1, #2, and #3 are 159%, 167%, and 182% of the control device, respectively. The corresponding calculated incident light intensities for these configurations are 158%, 162%, and 179% of the control, respectively. The slight discrepancies between the measured and calculated values are likely attributable to uncertainties in parameters such as the self-absorption coefficient. Both the incident light intensity and the current density are influenced by the outcoupling efficiency and the X-ray energy deposition rate. Although the Al-coated PET film (#2) has lower reflectivity than the aluminum foil (#1), its reduced X-ray absorption leads to a higher current density in the RL battery. All configurations exhibit consistent trends between measurement and simulation, demonstrating the validity of the optimization strategy and the accuracy of the device model.

C. Optocoupler to enhance the light extraction

The introduction of a reflective film effectively reduces optical losses from the top and side surfaces. However, it also

elongates the average light path within the scintillator, leading to increased self-absorption losses. As depicted in Fig. 6(a), an optical coupler adhesive (OA) layer was introduced between the $Cs_3Cu_2I_5$: Tl scintillator and the GaInP PV unit to enhance light extraction from the scintillator and mitigate the extra self-absorption loss simultaneously. The OA layer reduces the intensity of total internal reflection and hence increases the outcoupling light intensity. Fig. 6(b) shows the calculated outcoupling efficiency of RL battery as a function of the refractive index of OA layer using the Geant4 model. It can be seen that the outcoupling efficiency increases with the increasing refractive index of OA layer when the refractive index is smaller than 1.8, the refractive index of $Cs_3Cu_2I_5$: Tl scintillator (1.79). When the refractive index of OA layer is larger than 1.8, the total internal reflection at the interface between then scintillator and PV unit disappears and the outcoupling efficiency becomes constant. In this study, EGZ-SD65WH optical silicone grease, which has a refractive index of 1.46, was selected as the OA material to improve optical matching. The calculated outcoupling efficiency with silicone grease was 38.4%, representing a 67.7% increase compared to the battery without silicone grease.

As illustrated in the optical physical process in Fig. 6(a), photons with large incident angles undergo total internal reflection (TIR) at the interface between the scintillator and the PV unit. The introduction of an OA layer improves refractive index matching and enlarges the critical angle for light extraction from the scintillator. Fig. 6(c) displays the angular distribution of light emitted from the $Cs_3Cu_2I_5$: Tl scintillator with and without the OA layer. Without the OA layer, only photons with incident angles less than 34° can escape the scintillator. The OA layer expands the escape angle from 34° to 56° , thereby significantly improving the outcoupling efficiency. Fig. 6(d) further compares the angular radiant intensity of the scintillator with and without the OA layer. The results exhibit a Lambertian emission profile, with peak intensity at 0° (normal) and an intensity that drops off as the viewing angle increases. A noticeable increase in radiant intensity is observed across all angles. Fig. 6(e) presents the measured current density–voltage (J–V) characteristics of the RL battery with and without the OA layer under X-ray irradiation of an X-ray tube biased at 50 kV and 1 mA tube current. The short current density of the device with the OA layer exhibits a substantial improvement (an increase of 65.6%), indicating the perfect alignment with the experimentally measured 67.7% improvement in outcoupling efficiency. These results convincingly demonstrate the efficacy of the OA layer in improving light extraction and overall performance of the RL battery.

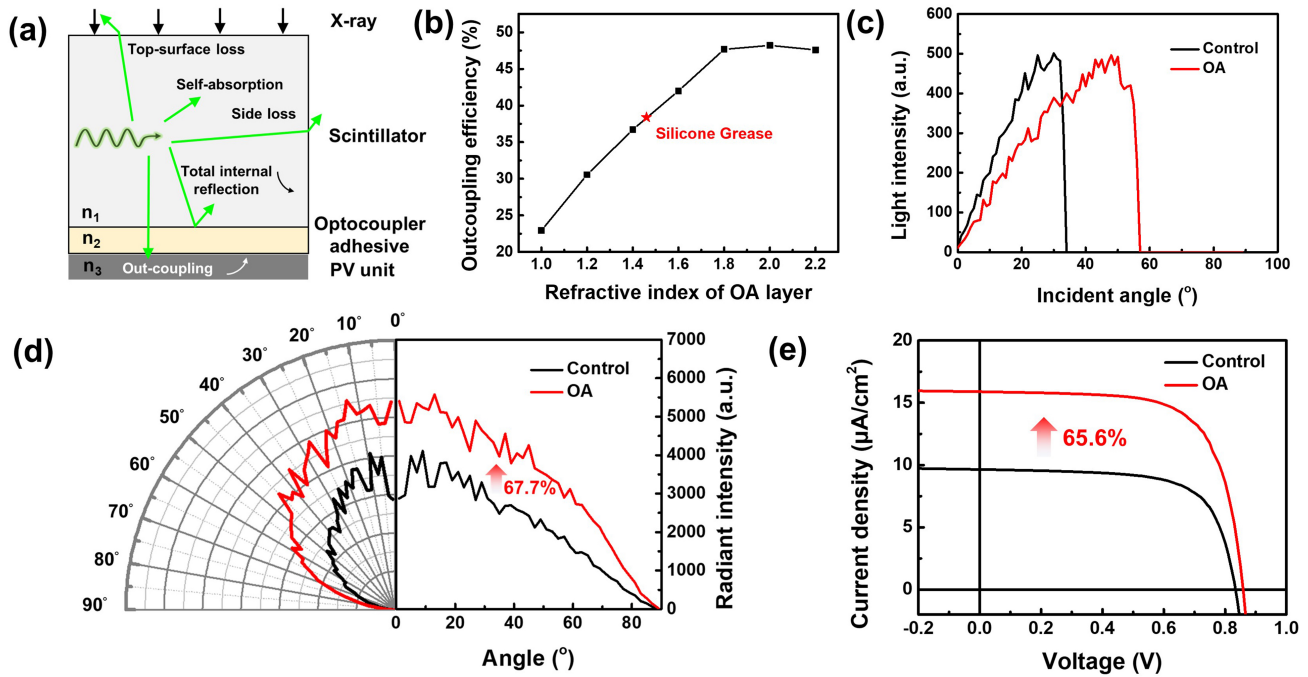


Fig. 6. (a) Schematic diagram of $Cs_3Cu_2I_5$: Tl - based X-ray RL battery with an optocoupler adhesive (OA) layer; (b) Calculated outcoupling efficiency of RL battery as a function of the refractive index of OA layer, marked with the silicone grease with a refractive index of 1.46; (c) Calculated angular distribution of lights exiting the $Cs_3Cu_2I_5$: Tl scintillator with and without OA layer; (d) Calculated angular radiant intensity of $Cs_3Cu_2I_5$: Tl scintillator with and without the optical coupling adhesive (OA) layer; (e) J-V curves of the RL battery with and without OA layer measured under the radiation of an X-ray tube biased at 50 kV and with a tube current of 1 mA.

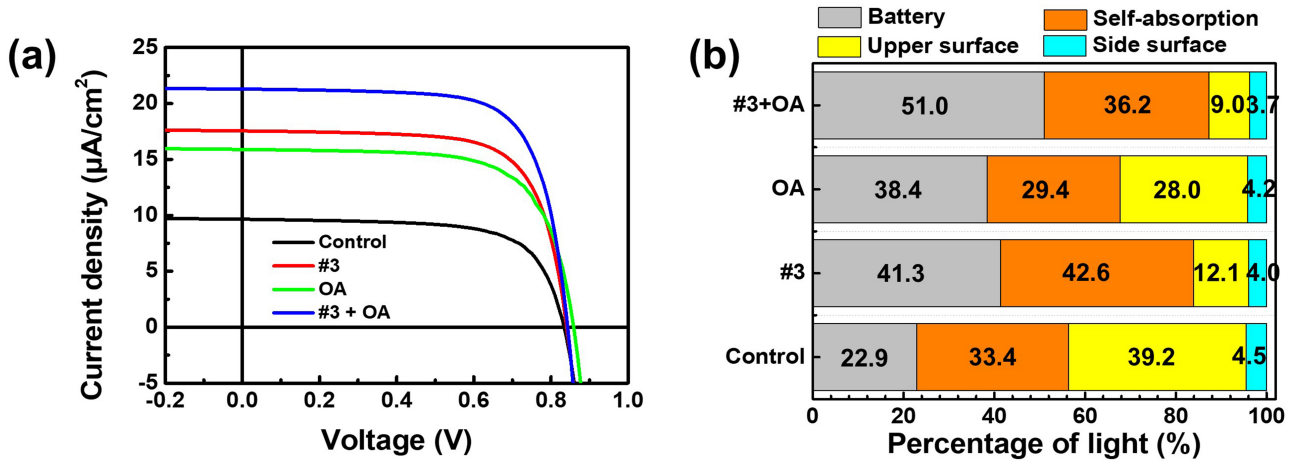


Fig. 7. (a) J-V curves of the RL battery with four battery configurations including (i) control (no addition layers), (ii) with a Organic reflection film (#3), (iii) with an optocoupler adhesive (OA) layer, and (iv) with both Organic reflection film and OA layers, measured under the radiation of an X-ray tube biased at 50 kV and with a tube current of 1 mA; (b) Quantitative analysis of different optical loss mechanisms in the four battery configurations.

TABLE 2. Output parameters of RL batteries with 4 configurations under 50 kV X-ray

Sample	$J_{sc}(\mu A/cm^2)$	$V_{oc}(V)$	FF(%)	$P_{out}(\mu W/cm^2)$	$\eta(\%)$
Control	9.6	0.834	68.5	5.51	0.92
#3	17.5	0.841	70.8	10.4	1.75
OA	15.9	0.859	68.7	9.38	1.58
#3+OA	21.3	0.843	71.7	12.9	2.15

D. Performance enhancement with both reflective and OA layer

The performance of the RL battery incorporating both reflective film (#3) and an optical adhesive (OA) layer was evaluated the overall performance, as shown in Fig. 7(a). The cur-

rent density–voltage (J–V) curves demonstrate a further increase in current when both layers are applied. Detailed output parameters for all four configurations under 50 kV X-ray irradiation are listed in Table. 2. The battery equipped with both the #3 reflective film and the OA layer achieves a short-circuit current density (J_{sc}) of $\mu A/cm^2$, a maximum output power density (P_{out}) of $12.9 \mu W/cm^2$, and an energy conversion efficiency of 2.15%, representing a 133.7% improvement over the control device. FFig. 7(b) presents a quantitative analysis of the optical loss mechanisms for the four configurations, obtained from the Geant4 simulation. The incorporation of the OA layer substantially enhances light extraction from the bottom interface and reduces self-absorption loss by shortening the internal optical path within the scintillator. The combination of the reflective film and OA layer reduces the top-surface loss to 9.0% and the self-absorption loss to 36.2%, leading to the outcoupling efficiency of 51.0%, which is 222.2% of the control value and closely matches the experimental value of 221.8%. In summary, the key strategies for improving optical coupling efficiency in RL batteries involve reducing the internal optical path length to minimize self-absorption losses and suppressing light leakage at the top and side surfaces.

IV. CONCLUSION

In summary, we have developed an effective method to improve the light collection efficiency in scintillator and suc-

cessfully doubled the power efficiency of X-ray RL batteries via tuning the optical field. Geant4 simulation results demonstrate that only one out of four photons can enter the PV units in RL batteries. The introduction of organic reflective layers and optical silicone grease as an optocoupler adhesive successfully achieved a significant improvement in outcoupling efficiency of scintillator from 22.9% to 51.0%, resulting from the reduction of the self-absorption and surface leakage loss. Based on a $Cs_3Cu_2I_5$: Tl scintillator and a spectrally matched GaInP unit, the optimized RL battery demonstrated an ultrahigh efficiency of 2.15% and an exceptional power density of $12.9 \mu W/cm^2$ under the radiation of a tungsten-target X-ray tube at a 50kV tube voltage and 1.0mA tube current. Monte Carlo simulations confirmed the effectiveness of this strategy in suppressing self-absorption and light leakage losses, with theoretical analysis predicting a 222.2% improvement in optical coupling efficiency, which aligns closely with experimental results (221.8% improvement). These findings highlight the critical role of tuning optical field inside the scintillator for boosting battery efficiency, underscore the substantial application potential of RL batteries, and provide a viable strategy for further performance enhancement.

- [1] K. Li, C. Yan, J. Wang et al., Micronuclear battery based on a coalescent energy transducer. *Nature* **633**, 811-815 (2024). [10.1038/s41586-024-07933-9](https://doi.org/10.1038/s41586-024-07933-9)
- [2] T. Jiang, S. Li, W. Yao et al., High-efficiency ^{90}Sr radiophotovoltaic cells based on waveguide light concentration structure. *LIGHT-SCI APPL* **14**, 214 (2025). [10.1038/s41377-025-01875-1](https://doi.org/10.1038/s41377-025-01875-1)
- [3] A. N. Kandala, S. Wang, J. E. Blecha et al., Millimeter-scale radioluminescent power for electronic sensors. *iScience* **28**, 111686 (2025). [10.1016/j.isci.2024.111686](https://doi.org/10.1016/j.isci.2024.111686)
- [4] T. Jiang, S. Li, X. Li et al., Radioluminescent Nuclear Battery for the Application of Self-Powered Sensors, In 2024 Ieee Sensors, 2024: 1-4. [10.1109/sensors60989.2024.10784778](https://doi.org/10.1109/sensors60989.2024.10784778)
- [5] A. B. Phatangare, S. V. Bhoraskar, S. S. Dahiwalé et al., Novel Nuclear Batteries Based on Radioluminescence. *Energy Tech.* **10**, 2200285 (2022). [10.1002/ente.202200285](https://doi.org/10.1002/ente.202200285)
- [6] H.-J. He, Y.-C. Han, X.-Y. Wang et al., Enhancing betavoltaic nuclear battery performance with 3D P+PNN+ multi-groove structure via carrier evolution. *Nucl. Sci. Tech.* **34**, 181 (2023). [10.1007/s41365-023-01331-y](https://doi.org/10.1007/s41365-023-01331-y)
- [7] Z. Ding, T.-X. Jiang, R.-R. Zheng et al., Quantitative modeling, optimization, and verification of ^{63}Ni -powered betavoltaic cells based on three-dimensional ZnO nanorod arrays. *Nucl. Sci. Tech.* **33**, 144 (2022). [10.1007/s41365-022-01127-6](https://doi.org/10.1007/s41365-022-01127-6)
- [8] X.-Y. Li, J.-B. Lu, R.-Z. Zheng et al., Comparison of time-related electrical properties of PN junctions and Schottky diodes for ZnO-based betavoltaic batteries. *Nucl. Sci. Tech.* **31**, 18 (2020). [10.1007/s41365-020-0723-y](https://doi.org/10.1007/s41365-020-0723-y)
- [9] Y. Zhao, C. Zhao, H. Li et al., New member of micro power sources for extreme environmental explorations: X-ray-voltaic batteries. *Appl. Energy* **353**, 122103 (2024). [10.1016/j.apenergy.2023.122103](https://doi.org/10.1016/j.apenergy.2023.122103)
- [10] C. Zhao, F. Y. Liao, K. Z. Liu et al., Breaking the myth: Wide-bandgap semiconductors not always the best for betavoltaic batteries. *Appl. Phys. Lett.* **119**, 153904 (2021). [10.1063/5.0068269](https://doi.org/10.1063/5.0068269)
- [11] C. Qian, H. Guo, C. Han et al., Design of High-Efficiency SiC Betavoltaic Battery Structures With Reduced Impact of Near-Surface Recombination Based on Accurate Modeling. *IEEE T. Electron Dev.* **69**, 7141-7146 (2022). [10.1109/ted.2022.3216974](https://doi.org/10.1109/ted.2022.3216974)
- [12] C. Zhao, J. W. Ren, L. Lei et al., Tenfold efficiency improvement of x-ray radioluminescent batteries basing on GAGG:Ce single crystal scintillators. *Appl. Phys. Lett.* **119**, 223901 (2021). [10.1063/5.0073048](https://doi.org/10.1063/5.0073048)
- [13] C. Zhao, J. W. Ren, L. lei et al., X-ray radioluminescent battery with near milliwatt output power using CsI:Tl single crystal scintillator. *Appl. Phys. Lett.* **121**, 123906 (2022). [10.1063/5.0109011](https://doi.org/10.1063/5.0109011)
- [14] D. D. Yang, Z. H. Xu, C. H. Gong et al., Armor-like passivated $CsPbBr_3$ quantum dots: boosted stability with hand-in-hand ligands and enhanced performance of nuclear batteries. *J. Mater. Chem. A* **9**, 8772-8781 (2021). [10.1039/d0ta12365j](https://doi.org/10.1039/d0ta12365j)
- [15] Z. H. Xu, Z. R. Zhang, K. A. A. Gamage et al., Synergistic enhancement of CdSe/ZnS quantum dot and liquid scintillator for radioluminescent nuclear batteries. *Int. J. Energy Res.* **45**,

- 12195-12202 (2020). [10.1002/er.6213](https://doi.org/10.1002/er.6213)
- [16] Z. H. Xu, X. B. Tang, Y. P. Liu et al., *CsPbBr₃* Quantum Dot Films with High Luminescence Efficiency and Irradiation Stability for Radioluminescent Nuclear Battery Application. *ACS Appl. Mater. Interfaces* 11, 14191-14199 (2019). [10.1021/ac-sami.9b02425](https://doi.org/10.1021/ac-sami.9b02425)
- [17] D. Liang, Z. Xu, D. Yang et al., Ultra-stable *CsPbBr₃*-embedded polymer films for spectrally tunable X-ray nuclear batteries and flexible radiation imaging applications. *J. Mater. Chem. C* 12, 17115-17121 (2024). [10.1039/d4tc02477j](https://doi.org/10.1039/d4tc02477j)
- [18] W. Chen, X. B. Tang, Y. P. Liu et al., Radioluminescent nuclear battery containing *CsPbBr₃* quantum dots: Application of a novel wave-shifting agent. *Int. J. Energy Res.* 43, 4520-4533 (2019). [10.1002/er.4580](https://doi.org/10.1002/er.4580)
- [19] Z. R. Zhang, X. B. Tang, Y. P. Liu et al., Application of liquid scintillators as energy conversion materials in nuclear batteries. *SENSOR ACTUAT A-PHYS* 290, 162-171 (2019). [10.1016/j.sna.2019.03.024](https://doi.org/10.1016/j.sna.2019.03.024)
- [20] W. Chen, X. Tang, Y. Liu et al., Novel radioluminescent nuclear battery: Spectral regulation of perovskite quantum dots. *Int. J. Energy Res.* 42, 2507-2517 (2018). [10.1002/er.4032](https://doi.org/10.1002/er.4032)
- [21] X. Song, L. Liu, P. Wan et al., Ultrabroad Dynamic All-Solid-State Radiation Dose Detector Based on a 0D *Cs₃Cu₂I₅* Perovskite-Like Single Crystal. *ACS Appl. Electron. Mater.* 5, 6805-6812 (2023). [10.1021/acsaelm.3c01256](https://doi.org/10.1021/acsaelm.3c01256)
- [22] S. Cheng, M. Nikl, A. Beitlerova et al., Ultrabright and Highly Efficient All-Inorganic Zero-Dimensional Perovskite Scintillators. *Adv. Opt. Mater.* 9, 2100460 (2021). [10.1002/adom.202100460](https://doi.org/10.1002/adom.202100460)
- [23] Q. Wang, C. E. Wang, Z. Wang et al., Achieving Efficient Neutron and Gamma Discrimination in a Highly Stable ⁶Li-Loaded *Cs₃Cu₂I₅* Perovskite Scintillator. *J. Phys. Chem. Lett.* 13, 9066-9071 (2022). [10.1021/acs.jpcllett.2c02643](https://doi.org/10.1021/acs.jpcllett.2c02643)
- [24] Q. Wang, Q. Zhou, M. Nikl et al., Highly Resolved X-Ray Imaging Enabled by In(I) Doped Perovskite-Like *Cs₃Cu₂I₅* Single Crystal Scintillator. *Adv. Opt. Mater.* 10, 2200304 (2022). [10.1002/adom.202200304](https://doi.org/10.1002/adom.202200304)
- [25] Q. Gao, Q. Wang, W. Li et al., Effects of rare earth codoping on the optical and scintillation properties of *Cs₃Cu₂I₅* : *Tl* single crystals. *J. Cryst. Growth* 636, (2024). [10.1016/j.jcrysgro.2024.127717](https://doi.org/10.1016/j.jcrysgro.2024.127717)
- [26] Q. Gao, Q. Wang, Y. Wu, Segregation of Tl ions in Bridgman-grown *Cs₃Cu₂I₅* : *Tl* single crystal scintillators. *J. Cryst. Growth* 645, (2024). [10.1016/j.jcrysgro.2024.127840](https://doi.org/10.1016/j.jcrysgro.2024.127840)
- [27] Q. Wang, C. Wang, H. Shi et al., Exciton-harvesting enabled efficient charged particle detection in zero-dimensional halides. *LIGHT-SCI APPL* 13, (2024). [10.1038/s41377-024-01532-z](https://doi.org/10.1038/s41377-024-01532-z)
- [28] Q. Wang, M. Nikl, S. Cheng et al., Undoped and Tl-Doped *Cs₃Cu₂I₅* Thin Films as Potential X-ray Scintillators. *Phys. Status Solidi* 15, 2100422 (2021). [10.1002/pssr.202100422](https://doi.org/10.1002/pssr.202100422)
- [29] Y. Wu, D. Sun, G. Ren et al., Centimeter-sized *Cs₃Cu₂I₅* Single Crystal: Synthesized by Low-cost Solution Method and Optical and Scintillation Properties. *J INORG MATER* 37, 1129 (2022). [0.15541/jim20220028](https://doi.org/10.15541/jim20220028)
- [30] X. M. Li, J. X. Chen, D. D. Yang et al., Mn(2+) induced significant improvement and robust stability of radioluminescence in *Cs₃Cu₂I₅* for high-performance nuclear battery. *Nat. Commun.* 12, 3879 (2021). [10.1038/s41467-021-24185-7](https://doi.org/10.1038/s41467-021-24185-7)
- [31] R. Gao, X. Ouyang, Q. Wang et al., High-Performance Radioluminescent Nuclear Battery Based on Ultrabright *Cs₃Cu₂I₅* : *Tl* Single Crystal Scintillator. *IEEE Trans. Nucl. Sci.* 71, 2530-2535 (2024). [10.1109/tns.2024.3476119](https://doi.org/10.1109/tns.2024.3476119)
- [32] D. Liang, Z. Xu, Z. Yang et al., Ultra 40% optical and electrical performance enhancement of silver nanosphere array-structured radioluminescent nuclear batteries. *SENSOR ACTUAT A-PHYS* 380, 116007 (2024). [10.1016/j.sna.2024.116007](https://doi.org/10.1016/j.sna.2024.116007)
- [33] Y. He, Z. Xu, H. Wang et al., Enhanced radioluminescence and improved radioluminescent nuclear battery output performance more than 50% with *SiO₂* nanosphere coating. *J. Lumin.* 255, 119600 (2023). [0.1016/j.jlumin.2022.119600](https://doi.org/10.1016/j.jlumin.2022.119600)
- [34] T. Jiang, Z. Ding, R. Zheng et al., ⁶³Ni-based radioluminescent isotope cells with enhanced photon transport interfaces. *J SCI-ADV MATER DEV* 8, 100611 (2023). [10.1016/j.jsamd.2023.100611](https://doi.org/10.1016/j.jsamd.2023.100611)
- [35] C. Zhao, H. Li, Y. Liu et al., Energy loss quantification and efficiency enhancing strategies for radioluminescent batteries. *Appl. Phys. Lett.* 127, 223902 (2025). [10.1063/5.0307280](https://doi.org/10.1063/5.0307280)